On two mechanisms of the domain structure of ventricular fibrillation

V.N. Biktashev[1,2], A.V. Holden [1],
S.F. Mironov[3], A.M. Pertsov[3] and A.V. Zaitsev[3]

Submitted to IJBC: 2000/08/11

[1]School of Biomedical Sciences, University of Leeds, Leeds LS2 9JT, UK
[2]Division of Applied Mathematics, School of Mathematical Sciences, University of Liverpool, Liverpool, UK. On leave from: Institute for Mathematical Problems in Biology, Pushchino, 142292, Russia
[3]Department of Pharmacology, SUNY Health Science Center, 750 East Adams St., Syracuse, NY 13210, USA

Abstract

Analysis of optically recorded irregular electrical wave activity on the surface of the heart during experimentally induced fibrillation reveals a strong local temporal periodicity. The spatial distribution of the dominant temporal frequencies of excitation has a domain organization. The domains are large ($\approx 1\,\mathrm{cm}^2$) and they persist for minutes. We demonstrate that these data can be reproduced in a two-dimensional excitable medium governed by the FitzHugh-Nagumo equations with a spatial inhomogeneity. We identified two potential mechanisms that may contribute to the observed experimental dynamics: coexistence of stable spiral waves with non-commensurate frequencies of rotation, and Wenckebach-like frequency division from a single spiral source due to inhomogeneity. The number of domains is *not* an index of the number of wave sources. Both mechanisms reproduce the uniformity of the dominant frequency within individual domains and sharp boundaries between domains. The possibility of distinguishing between different mechanisms using Lissajous figures is discussed.

1 Introduction

It is now possible to map optically, using voltage sensitive dyes, the electrical activity on the surfaces of cardiac muscle with a high spatial and temporal resolution. Such mapping has advanced significantly the experimental study of fibrillation. This has revealed a high degree of spatio-temporal organisation of electrical activity during experimentally induced fibrillation [Gray, Pertsov & Jalife 1998, Witkowski, Leon, Penkoske, Giles, Spano, Ditto & Winfree 1998]. Quantitative analysis of the excitation patterns has led to the observation that the dominant frequency of oscillations has a domain structure, the dominant frequency being approximately uniform within one domain but different in different domains, and the boundaries between the domains being quite sharp, with the domains persisting over tens of seconds *i.e.* hundreds of times longer than the approximate periodicity of the local oscillations [Biktashev, Holden, Mironov, Zaitsev & Pertsov 1999*b*, Zaitsev, Berenfeld, Jalife, Mironov & Pertsov 2000]. Interpretation of fibrillation as re-entry breakup cascades, be it due to two-dimensional [Panfilov & Holden 1990] or three-dimensional [Biktashev 1998, Fenton & Karma 1998] mechanisms, implies mobility of the reentry blocks, spiral cores or scroll filaments. This is hardly consistent with the observed persistence of the frequency domain structure in these experiments. Thus, the newer evidence of order in fibrillation, based on statistical analysis of high-resolution data, seemingly contradicts the traditional picture of the disorder of fibrillation, based on low-resolution maps, single site electrograms or the ECG. This contradiction requires a theoretical explanation.

In this paper, we explore possible mechanisms of the domain structure. Our basic assumption is that fibrillation is caused by pinned re-entrant vortices[Winfree 1994, Zaitsev et al. 2000]. As a single spiral wave would only produce a periodic (monomorphic) pattern, some modification is required to explain the polymorphic behaviour. We consider two hypothesis:

M: There are two (or more) different re-entry vortices with different periods, and the domains of influence of the vortices are the dominant frequency domains.

W: There is essentially only one re-entry vortex, but its period is shorter than the minimal propagation period in some parts of the tissue, so in those parts intermittent conduction causing simple rational frequency division is observed. In cardiology this is described as Wenckebach frequency division.

Note that the hypothesis M is not quite trivial. It is a widespread belief that two or more periodic sources of waves in an excitable medium cannot coexist for a long time, as the fastest source should entrain all others. The mechanism of such entrainment is based on the observation that the excitation waves, in the head-on collisions, annihilate in the ratio 1:1. The entrainment of slower sources has been discussed theoretically [Gelfand & Tsetlin 1960, Pertsov & Ermakova 1988*b*, Winfree 1991, Biktashev 1997, Vinson 1998, Xie, Qu, Weiss & Garfinkel 1999] and demonstrated experimentally in the Belousov-Zhabotinsky reaction medium [Krinsky & Agladze 1983]. This sometimes leads to a natural but hastily drawn conclusion that coexistence of sources of different frequencies in the same medium is

impossible [Xie et al. 1999]. Entrainmentby the fastes source, however, assumes a relative homogeneity of the medium. If the medium is strongly nonhomogeneous, then it is conceivable that the waves of the faster source may be simply unable to penetrate the more refractory part of the medium where the slower source is located. As a result, some excitation waves annihilate by themselves without colliding with other waves, and no entrainment will occur. Note that different frequencies of spiral waves implies an inhomogeneity of properties, in particularl the refractoriness.

To substantiate the two hypotheses of frequency domain formation, we reproduce the phenomenon by numerical simulations, using the simple FitzHugh-Nagumo caricature of the excitable tissue. The reason for choosing this model rather than a more realistic biophysically detailed model, is that currently it is not known which particular parameter inhomogeneities are most important. Using the simulations, we identify the key features of the excitation patterns corresponding to each of the two mechanisms, and apply this to the patterns observed in the isolated tissue experiments. The result is that both hypotheses are consistent with the experimental data. Moreover, both mechanisms may be involved, either simultaneously, or one mechanism may switch to the other. In all cases a small number of re-entrant sources in an inhomogeneous medium is sufficient to reproduce the characteristics of the experimentally observed domains.

2 Methods

Numerical model Both hypotheses require a macroscopic inhomogeneity of the tissue. It is well known that in an inhomogeneous medium re-entrant vortices tend to drift [Pertsov & Ermakova 1988*a*, Fast & Pertsov 1990, Biktashev & Holden 1995]. To prevent this drift and so produce numerical simulations of stationary rotating vortices in an inhomogeneous medium, we exploited the effect of pinning to localised inhomogeneities [Vinson, Pertsov & Jalife 1994, Pertsov, Cabo, Baxter, Gray, Davidenko & Jalife 1994, Xie et al. 1999]. We used the following inhomogeneous variant of the FitzHugh-Nagumo system:

$$\begin{aligned} \frac{\partial u}{\partial t} &= \epsilon_u^{-1}(\mathbf{r})(u - u^3/3 - v) + \nabla^2 u \\ \frac{\partial v}{\partial t} &= \epsilon_v(\mathbf{r})(u + \beta - \gamma v), \end{aligned} \tag{1}$$

in a rectangular region $\mathbf{r} \in [0, X] \times [0, Y]$, $X = 30$, $Y = 12$, with impermeable boundaries, for $\beta = 0.68$ and $\gamma = 0.5$. Parameters $\epsilon_{u,v}$ depended on $\mathbf{r}$, to represent spatial inhomogeneities (see Fig. 1):

$$\begin{aligned} \epsilon_v(\mathbf{r}) &= \epsilon/\chi(\mathbf{r}), \\ \epsilon_u(\mathbf{r}) &= \epsilon\chi(\mathbf{r}) \left(1 + K\exp\{-|(\mathbf{r} - \mathbf{r}_l)/\lambda_l|^2\} + K\exp\{-|(\mathbf{r} - \mathbf{r}_r)/\lambda_r|^2\}\right), \\ \chi(\mathbf{r}) &= = 1 + \frac{1}{2}\left(1 + \tanh\left(\frac{x - x_b}{w}\right)\right)(k - 1). \end{aligned} \tag{2}$$

The function $\chi(\mathbf{r})$ provided a macroscopical inhomogeneity, namely, a non-specific k-fold slowdown of all dynamic variables in the right hand part of the medium compared to the left, and the terms $K\exp()$ in ϵ_u provided a localised suppression of excitability in two 'holes', the regions with radii of the order λ_l. Figure 1 illustrates the distribution of ϵ_u and ϵ_v in the medium, for two different parameter sets used in the numerics. These sets were different in parameters k and w: $k=(1+\sqrt{5})/2\approx 1.618$ and $w=3$ (producing a stronger but smoother inhomogeneity) and $k=\sqrt{2}\approx 1.414$ and $w=0$ (producing a slighter but sharper, stepwise inhomogeneity). Other parameters were $\epsilon=0.3$, $K=100$, $\lambda_l=0.6$, $\lambda_r=\lambda_l\sqrt{k}$, $\mathbf{r}_l=(0.15X,0.5Y)$, $\mathbf{r}_r=(0.8X,0.5Y)$, and $x_b=0.4X$.

The initial conditions were established as follows. A spiral wave was initiated in a homogeneous medium ($k=1$, $K=0$). The dynamical variables $U(\phi)=u(\mathbf{r},2\pi t/T)$, $V(\phi)=v(\mathbf{r},2\pi t/T)$ were recorded at a point $\mathbf{r}$ far from the core of the spiral, for one rotation period, $t\in[0,T]$. This recording was used to create initial conditions for the inhomogeneous medium, $u(\mathbf{r},0)=U(\phi)$, $v(\mathbf{r},0)=V(\phi)$, where the distribution of the phase ϕ was specified to provide either one spiral wave,

$$\phi=|\mathbf{r}-\mathbf{r}_l|/\Lambda_l-\arg(\mathbf{r}-\mathbf{r}_l), \tag{3}$$

or two spiral waves,

$$\phi=\max\left\{|\mathbf{r}-\mathbf{r}_l|/\Lambda_l-\arg(\mathbf{r}-\mathbf{r}_l),-|\mathbf{r}-\mathbf{r}_r|/\Lambda_r+\arg(\mathbf{r}-\mathbf{r}_r)\right\}, \tag{4}$$

around the inexcitable holes $\mathbf{r}_l$, $\mathbf{r}_r$. Here $\Lambda_l=3$, $\Lambda_r=\Lambda_l\sqrt{k}$, and $\arg(\mathbf{r})$ is defined as the angle made by vector $\mathbf{r}$ with the x-axis (counter-clockwise being positive).

Simulations were performed with spatial step 0.2 space units (s.u.) of (1) and output data were sampled with interval 0.64 time units of (1). The value of the variable u in the solutions to (1) was taken as an equivalent of the optical signal in the experimental procedure described below. The time unit of (1) was assumed to correspond to 13 ms., as if the numerical data were sampled with the frequency 120 Hz; this provides a rough correspondence of the oscillations frequencies observed in experiment and in numerics.

Experimental procedures The numerical simulations were compared with experimental results. Experimental visualisations of electrical activity were from the endo- and epicardial surfaces of pieces of fibrillating sheep ventricular wall (5-11 mm thick) that had been excised and perfused via the coronary arteries, and superfused with oxygenated physiological saline containing a drug (diacetyl monoxime), that blocked contraction, and a potential-sensitive dye (di-4-ANEPPS). The video images were obtained with a spatial resolution of 0.2 to 0.5 mm and a temporal resolution of 2.5 to 8.3 ms and stored with a 8-bit precision. The length of time series was from 2 to 10 s, and the size of preparation was about 3 cm. More technical details can be found in [Pertsov, Davidenko, Salomonsz, Baxter & Jalife 1993, Biktashev, Holden, Mironov, Pertsov & Zaitsev 1999*a*, Zaitsev et al. 2000]. Irregular, self-sustained re-entrant propagation, which we assumed as an experimental model of fibrillation, was induced in a resting tissue preparation by rapid electric pacing.

2.1 Data processing

The processing included calculation of pseudo-ECG, and finding pointwise Fourier spectra with subsequent pointwise bandpass filtering of the signals and calculating the spatial distribution of powers of the frequency bands.

Pseudo-ECG The pseudo-ECG signals were calculated from the experimental and simulation data, $u(x, y, t)$, by simple summation,

$$E(t) = \iint u(x, y, t)\,\mathrm{d}x\mathrm{d}y. \tag{5}$$

Both the real ECG and the calculated $E(t)$ are integral characteristics of electrical activity; $E(t)$ has an advantage that it can be easily obtained directly from optical mapping data, and from the results of numerical simulations, thus providing a uniform approach to both types of datasets.

Fourier spectra We performed a pointwise discrete Fourier transform on both the simulation and tissue experimental data,

$$\tilde{u}(x, y, f) = \mathcal{F}[u(x, y, t)] \tag{6}$$

to obtain the cumulative power spectra,

$$P(f) = \iint |\tilde{u}(x, y, f)|^2\,\mathrm{d}x\,\mathrm{d}y. \tag{7}$$

Note that a cumulative power spectrum obtained by (7) is a spectrum of the whole signal, *not* a power spectrum of the pseudo-ECG (5).

Filtering Given the frequencies of the main peaks and peak widths, the signals were then filtered to one of the two or three windows,

$$W_j(f) = \exp\left(-Q_j(1 - f/f_j)^4\right), \tag{8}$$

where f_j, $j = 1, 2(, 3)$ are the central frequencies of the windows, and Q_j are coefficients representing filtering quality. Parameters f_j and Q_j were chosen based on the visual analysis of frequency spectra of the experimental or numerical data, so that each window is reasonably wide but covers only one frequency peak.

Frequency band power distributions The distribution of the power of the frequency band j was computed as

$$B_j(x, y) = \int |\tilde{u}(x, y, f)|^2 W_j(f)\,\mathrm{d}f \tag{9}$$

and these distributions were then visualised using colour-coding, so that value of $B_j(x, y)$ was represented by intensity of j-th (red, green or blue) colour component of the hue at the point with coordinates (x, y).

3 Results

3.1 Frequency domains in experimental fibrillatory patterns

Figures 2 and 3 illustrate the frequency domain structure in experimental fibrillatory patterns. These are relatively simple patterns, with only two different dominant frequencies; usually more complicated patterns are observed, as in Fig. 4.

On Figs. 2, 3 and 4 , the top two plots are the pseudo-ECG $E(t)$ and cumulative power spectrum $P(f)$. Experimental data demonstrated a smooth shape of the recorded action potential, which produced virtually no higher harmonics, and the main peaks were easily identifiable, though often partially overlapping, as in Fig. 2. The large colour panel is the frequency domain map: the spatial distribution of the frequency bands power over the preparation $B_j(x, y)$, with higher frequency represented by blue and lower frequency by red, and the medium frequency on Fig. 4 green. The frequency windows $W_j(f)$ and power spectra of the whole preparation after bandpass filtering $P(f)W_j(f)$ are shown to the right of the domain map. Lower panels show individual signals from different points of the preparation, together with their power spectra.

The pseudo-ECG signals show polymorphic or fibrillatory activity, especially Figs. 3 and 4. Yet, the power spectra $P(f)$ clearly show two dominant frequencies for Figs. 2 and 3 and three for Fig. 4. The feature of the total power spectrum in Fig. 2 is that the two bands overlap, and so it is not obvious that they correspond to different processes. Yet, in all three examples, on the frequency distribution $B_j(x, y)$ panel one can clearly see the large regions of pure colours, as well as narrower regions of mixed colours, where two- or three-frequency oscillations occur. The different frequencies of oscillations are spatially separated, in domains. This is confirmed by the analysis of time series recorded at different points. The power spectra of the signals from pure-colour domains hardly overlap, the signal from the lower-frequency domains often having a slight high-frequency component, and that the signal from the border zones, as (B) on Figs. 3 and 4, has both components. The ratio of the frequencies in Fig. 2 was $15 : 12.5 = 6 : 5$, in Fig. 3, $17 : 13 \approx 1.31 \approx 4 : 3$ and in Fig. 4 approximately $4 : 3 : 2$.

3.2 Simulation: mechanisms of the frequency domain formation

Mechanism M: multiple independent spiral waves. Figure 5 illustrates coexistence of two spiral waves in a model with the stronger inhomogeneity $k = 1.618$. The period of the spiral wave in the right half of the medium is longer than the period in the left half, but no entrainments occur because the waves from the left spiral cannot penetrate the right half as they either come in the excited/refractory phase, or just slightly advance the phase of the right spiral if they come during the excitable gap.

Despite the fact that there are only two stable spiral waves, the pseudo-ECG appears complicated, due to incommensurability of their periods. In order to compare the simulation results with the experiments, we processed the solution $u(x, y, t)$ in the same way as signals from the real experiments. The results are shown on Fig. 6. In this example, as well

as in all other numerical data, the frequency peaks were well separated, but higher harmonics present. Often, the second harmonic was more powerful than a main frequency peak. For this reason, visual pre-analysis of spectra was necessary to determine the dominant frequencies.

In the case of Fig. 6, the frequency bands are well separated, both in the frequency domain and in space. There is only a narrow border zone with mixed frequencies. The ratio of the frequencies here was close to the ratio of two small integers, $19.5 : 15 \approx 4 : 3$. Note, however, that the electrograms show no entrainment of one spiral by the other. This is because their cores are sufficiently far from the border separating their domains. In our computation, this independent rotation of spiral waves lasted a very long time. The stability of the spirals was enhanced by presence of inexcitable holes, to which the spiral cores were 'anchored' and did not drift (see [Vinson et al. 1994] for more about anchoring).

Another such example is shown on Figs. 7 and 8, where the ratio of the time constants was less, $k \approx 1.414$. In this case of the lower inhomogeneity, the two spiral waves persisted only for a limited time, about 22 revolutions of the slower spiral and 30 of the faster. After that an excitation wave from the left spiral propagated into the excitable gap of the right spiral, reached its core and pushed it onto the inexcitable boundary. Thereafter, the right part of the medium simply conducted two out of every three excitation waves, *i.e.* the frequency domains were due to the Wenckebach mechanism.

Mechanism W: one spiral wave and Wenckebach frequency division . This mechanism was observed in each of the models described above, by specifying one spiral wave in the faster part of the medium as initial condition. As the period of the spiral in the faster part in both cases is shorter than the refractory period of the slower part, Wenckebach frequency division occured. For model of Fig. 8, that was 2:3, i.e. two out of three waves propagated and every third wave was blocked.

Similar behaviour was observed in the numerical experiment with two spiral waves and $k \approx 1.414$, after the slower spiral terminated. Selected snapshots of the u field are shown on Fig. 9 and corresponding data analysis is given on Fig. 10. It can be seen that the influence of the higher frequency is present in the low-frequency zone, but it diminishes with the distance.

Transition from M to W. Figures 7, 8 and Figs. 9, 10 represent two different mechanisms during different stages of the same numerical experiment. This illustrates the possibility of transition from one mechanism to the other, M to W, and raises the question when such transition can happen. A simple phenomenological criterium can be suggested in the assumption that the core of the slower spiral wave is sufficiently far from the site where the Wenckebach blocks occur. Further into the slower part of the medium from this site, the faster source would appear as a source of modified frequency, *i.e.* frequency divided by the Wenckebach ratio. It is this frequency that will compete with the slower spiral in the slower part of the medium. Therefore, a sufficient condition of the instability of the mechanism M with respect to transition to W is: the Wenckebach-divided frequency

Figure	6	8	10	2	3
Frequency ratio	1.58	1.36	1.50	1.20	1.31
Sharp domain margins present	yes	yes	yes	yes	yes
Broad mixed frequency regions present	no	no	yes	yes	yes
Domains overlap coefficient	0.06	0.11	0.23	0.34	0.21
Recurrence seen in the Lissajous curve	no	no	yes	no	may be
Mechanism	M	M	W	M?	W?

Table 1: Diagnostic features of the two mechanisms

of the fast source should be higher than the frequency of the slower source. In other words, the Wenckebach ratio should be lower than the frequency ratio of the two spirals.

As applied to our two numerical experiments, this criterium predicts stability of the slow spirals in both cases. Indeed, in the stronger inhomogeneity of Figs. 5, 6 the spirals' frequency ratio was 1.58 whereas the Wenckebach ratio was found to be 2; and in the weaker inhomogeneity of Figs. 7–10 the spirals's frequency ratio was 1.36 with Wenckebach ratio 1.5.

However, in the second case, Figs. 7 and 9, the slower spiral has been annihilated. This happened because its core was too close to the domain boundary. Thus, in effective prediction of the stability is more difficult, as the above criterium of stability is only necessary but not sufficient. If mechanism M is metastable, its duration may vary greatly.

3.3 Comparative phenomenology of the two mechanisms.

Experimental fibrillation is obviously more complicated process than the numerical mechanisms considered above. This is, in particular, due to such factors as inhomogeneity, anisotropy and three-dimensionality of the real cardiac muscle. This makes the spiral waves invisible or at least unrecognizable on the surface excitation patterns in the majority of cases, and so direct comparison with the two mechanisms is impossible.

There are some robust features of the excitation patterns, however, which would be preserved despite the above mentioned factors; such as e.g. the periods of the re-entry sources. Is it possible to use such features to establish which of the two mechanisms, if any, is responsible for a particular excitation pattern?

In this section, we study some of these features, to see which of them can distinguish between the two mechanisms. These are summarised in the Table 1.

Frequency ratio. This is a would-be obvious criterium as for the mechanism W, this ratio must be equal to a ratio of two small integer numbers, whereas for the mechanism M it may be any real number, and therefore if a particular ratio happens to be that of two small integer, it is a strong indication of the Wenckebach mechanism. In practice, however, life is a bit more complicated as the precision with which the frequencies can be determined, is limited by the time length of the signal. For experimental data it is even more difficult

as the widths of the frequency peaks are broader and the precision of the main frequencies is less. In the examples considered, frequency ratios of numerical experiments Figures 6 and 8 are significantly different from nearest small-integer ratios, and for Fig. 10 it is exactly 3:2, so in theory this criterium works well. For real experimental data, the ratios are exactly 6:5 for Fig. 2 and very close to 4:3 for Fig. 3. This might mean that in both cases mechanism W takes place, or may be a result of a simple coincidence: one can see on these figures that the frequency bands are quite wide for these signals.

Domain boundaries. Figures 8 and 10 are convenient for comparative study of the two mechanisms, as both mechanisms take place in the same 'numerical preparation'. In the two-spiral regime Fig. 8 there is only a thin strip of mixed frequency on the border. In the one-spiral regime, the mixed frequency occupies the major part of the slow half of the medium. This is because the excitation waves propagating through the right part retain the "two passed — one missed" frequency division structure and thus the frequency component of their original source, and the inhomogeneity of their train is only slowly damped down by phase diffusion [Biktashev 1989]. Note that in both experimental patterns, Fig. 2 and 3, thin borders as well as large regions of mixed frequency were observed, but in Fig. 3(a), the penetration of high frequency (blue) into the predominantly low-frequency region (red) is less than in Fig. 2(a).

The location and sharpness of the domain borders does not coincide with the borders of the distribution of tissue parameters, which is clearly seen in the numerical experiments (see Fig. 11). In all four cases, the width of the domain boundary is approximately the same, *i.e.* about 3 space units, whereas the border of the medium parameters was 3 space units wide in one series and 0.2 space units (one computational step) wide in the other series. And in all four cases, the location of the domain borders was significantly displaced with respect to that of medium parameters, into the slower region, so that the domain border and the step in the medium parameters hardly overlap.

To measure the degree of overlap between the domain distributions, we calculated the overlap coefficient defined as the cosine between these distributions considered as vectors of L_2, i.e.

$$\sigma_{j,k} = \int B_j(x,y) B_k(x,y)\,\mathrm{d}x\,\mathrm{d}y \left(\int B_j(x,y)^2\,\mathrm{d}x\,\mathrm{d}y \int B_k(x,y)^2\,\mathrm{d}x\,\mathrm{d}y \right)^{-1/2} \qquad (10)$$

The values of this coefficient are presented int the Table; these agree with the results of visual analysis, i.e. it is larger for the maps where overlap is evident. Its values for the two real experiments are close to each other and are larger than those in numerical experiments. Thus, whereas the overlap coefficient might be a useful diagnostic quantity in principle, it is hardly suitable to reliably distinguish between the two mechanisms.

Lissajous figures. As we already mentioned, closeness of the ratio of the domain frequencies to that of two small integers could be a sign of frequency division, but is not very practical due to the limited length of experimental series and instability of experimental

frequencies, seen as large width of the experimental spectra. A classical way to distinguish between commensurate and incommensurate frequency ratios is the Lissajous curve, i.e. the graph of the two signals where the x coordinate is one signal and y coordinate is the other signal. This method, unlike simple numerical comparison of mean frequencies, has the additional advantage that it allows for variations in the signals frequencies as long as these are synchronous. Such variations may widen up the spectra. But the Lissajous figure only monitors the dependence of one signal on the other, and if the frequencies change synchronously then, ideally, the Lissajous figure does not change at all, or realistically, changes only slightly.

Lissajous curves for the numerical experiments described above are presented in Fig. 12.

This was done with filtered signals, computed using forward and inverse Fourier transforms as

$$u_f(x,y,t) = \mathrm{Re}\left(\mathcal{F}^{-1}\left[\tilde{u}(x,y,f)\sum_j W_j(f)\right]\right). \tag{11}$$

where $\tilde{u}(x,u,f)$ is the time-Fourier image (6) of the original signal $u(x,y,t)$, and W_j, $j=1,2$ are the frequency windows (8).

These Lissajous figures show a clear distinction between the commensurate, (b,d) and incommensurate, (a,c) cases. Disregarding a few loops corresponding to the transient in the beginning of the numerical experiment, panel (b) shows a bold figure which makes 2 up/down motions, e.g. two tops and two bottoms, per one horizontal motion, thus showing 2:1 commensurate frequencies. On panel (d), the transient is more pronounced, so we emphasise the main Lissajous figure showing one complete loop of it with filled circles. This figure has three maxima and minima in the vertical direction vs two maxima and minima in the horizontal direction, thus demonstrating frequency ration 3:2. The panels (a) and (c) do not have such structures and thus demonstrate independent signals.

The Lissajous figures for the tissue experiments shown on Figs. 2 and 3 could not be interpreted with such certainty, as their shapes were apparently smeared out by experimental noise and/or some non-stationary processes in the preparation, which was impossible to establish due to the shortness of the experimental series.

This approach, however, can be quite useful if the experimental data are obtained for a considerably longer time. This is illustrated for the experiment shown on Fig. 4. Figure 13 shows Lissajous figures of signals recorded at the three points A, B, and C in Fig. 4 chosen in three different domains. In this case, the synchronous character of these signals is evident. This figure also illustrates the necessity of the filtering the electrograms, as described in section 2: without such filtering, the synchrony would not be seen. To ensure that this synchrony is not an artifact of the filtering, we plotted similar figures for signals of exactly the same spectra but with randomised phases of the Fourier coefficients. These randomised Lissajous figures are also shown on Fig. 13. They look quite erratic. This proves that the true filtered data show genuine dependence, not reducible to their spectral properties only, and therefore, not due to the filtering. Thus, we can conclude that in this particular experiment, there probably was only one source, with frequency of 9.6 Hz, which

was divided in the ratio 2 : 3 and 1 : 2 in different parts of the preparation.

4 Discussion

Ventricular fibrillation is believed to be produced by re-entrant wave sources, where a single re-entrant source that generates spiral waves in thin, effectively two dimensional tissue, and scroll waves in thicker, three dimensional tissue, breaks down to generate new re-entrant sources. The observed surface patterns of excitation have been interpreted in qualitative terms as the surface manifestations of three-dimensional scroll waves within the ventricular wall [Biktashev, Holden, Mironov, Pertsov & Zaitsev 1998, Biktashev et al. 1999*a*]. During the course of fibrillation, the number of re-entrant sources increases with time, to fluctuate about some mean. In [Biktashev et al. 1998, Biktashev et al. 1999*a*] we have shown that the observed surface patterns of excitation in this preparation can be interpreted in qualitative terms as the surface manifestations of three-dimensional scroll waves within the ventricular wall, with the axis of the scroll filaments lying roughly parallel to the heart surfaces.

The domain structure seen in Figures 1, 2 and 9 is only apparent after Fourier transformation of the signals, and illustrates a local spatial order in the surface activity. The frequency resolution of the Discrete Fourier Transform is limited by the length of the time series analysed, and since fibrillation *in vivo* is a short-lived process the ratio of frequencies obtained from different points will always be between integers. However, the common occurence of simple integer ratios between the dominant frequencies of different domains is highly suggestive of a frequency division mechanism for the domains. The features of most of the tissue experiments can be reproduced by a single re-entrant source, with intermittent conduction through regions of spatial inhomogeneity producing frequency division; the features of all the tissue experiments can be reproduced by a small number of re-entrant sources and such frequency division. Thus the surface patterns of activity can be reproduced by one, or a few, re-entrant sources, combined with heterogeneity. In the tissue experiments the re-entrant sources will be within the ventricular wall. The ventricular wall has a laminar structure [LeGrice, Smaill, Chai, Edgar, Gavin & Hunter 1995], and the connections between neighbouring sheets of ventricular tissue might form the anatomical sites for the heterogeneity that produces the frequency division.

Implications for defibrillation Understanding the detailed processes occuring during actual examples of fibrillation is very important for the design of tools for defibrillation. In particular, the feasibility and realisation of low-voltage defibrillation by feedback driven resonant drift depends on there being only a small number of re-entrant sources [Biktashev & Holden 1995]. If there is only one re-entrant source, the problem which of the sources to control does not occur. If there are several apparent sources, but these are produced by frequency division from one source, it is necessary to identify that source. For example, for Fig. 4 it is clear that the feedback controlling its motion the should be based on the frequency band of the highest frequency component, that of 9.6 Hz.

Acknowledgements

This work was supported by grants from The Wellcome Trust (045192), EPSRC ANM (GR/L17139), Russian Foundation for Basic Research (96-01-00592) and National Heart and Blood Institute (HL39707).

References

Biktashev, V. N. (1989), 'Diffusion of autowaves. Evolution equation for slowly varying autowaves', *Physica D* **40**(1), 83–90.

Biktashev, V. N. (1997), Control of re-entrant vortices by electrical stimulation, *in* A. V. Panfilov & A. V. Holden, eds, 'Computational Biology of the Heart', John Wiley & Sons, Chichester, chapter 5, pp. 137–171.

Biktashev, V. N. (1998), 'A three-dimensional autowave turbulence', *Int. J. of Bifurcation and Chaos* **8**(4), 677–684.

Biktashev, V. N. & Holden, A. V. (1995), 'Resonant drift of autowave vortices in 2D and the effects of boundaries and inhomogeneities', *Chaos Solitons & Fractals* **5**(3,4), 575–622.

Biktashev, V. N., Holden, A. V., Mironov, S. F., Pertsov, A. & Zaitsev, A. (1999*a*), 'Three dimensional aspects of re-entry in experimental and numerical models of ventricular fibrillation', *Int. J. of Bifurcation and Chaos* **9**(4), 694–704.

Biktashev, V. N., Holden, A. V., Mironov, S. F., Pertsov, A. M. & Zaitsev, A. V. (1998), 'Three dimensional aspects of re-entry in two models of ventricular fibrillation', *J. Physiol.* **509P**(SISI), P139.

Biktashev, V. N., Holden, A. V., Mironov, S. F., Zaitsev, A. V. & Pertsov, A. M. (1999*b*), 'Intermittent conduction block can account for the spatial distribution of dominant frequencies during ventricular fibrillation', *J. Physiol.* **518P**, P38.

Fast, V. G. & Pertsov, A. M. (1990), 'Drift of vortex in myocardium', *Biofizika* **35**(3), 478–482. in Russian.

Fenton, F. & Karma, A. (1998), 'Vortex dynamics in three-dimensional continuous myocardium with fiber rotation: Filament instability and fibrillation', *Chaos* **8**(1), 20–47.

Gelfand, I. M. & Tsetlin, M. L. (1960), 'On continuous models of control systems', *Doklady Akademii Nauk SSSR* **131**(6), 1242.

Gray, R. A., Pertsov, A. M. & Jalife, J. (1998), 'Spatial and temporal organization during cardiac fibrillation', *Nature* **392**, 75–78.

Krinsky, V. I. & Agladze, K. I. (1983), 'Interaction of rotating waves in an active chemical medium', *Phyisca D* **8**, 50–56.

LeGrice, I. J., Smaill, B. H., Chai, L. Z., Edgar, S. G., Gavin, J. B. & Hunter, P. J. (1995), 'Laminar structure of the heart — ventricular myocyte arrangement and connective tissue architecture in the dog', *American Journal of Physiology — Heart and Circulatory Physiology* **38**(2), H571–H582.

Panfilov, A. V. & Holden, A. V. (1990), 'Self-generation of turbulent vortices in a 2-dimensional model of cardiac tissue', *Phys. Lett. A* **151**(1–2), 23–26.

Pertsov, A. & Ermakova, E. (1988*a*), 'Mechanism of the drift of a spiral wave in an inhomogeneous medium', *Biofizika* **33**(2), 338–342. in Russian.

Pertsov, A. M. & Ermakova, E. A. (1988*b*), 'Mechanism of the drift of a spiral wave in an inhomogeneous medium', *Biofizika* **33**(2), 338–342.

Pertsov, A. M., Cabo, C., Baxter, W. T., Gray, R. A., Davidenko, J. M. & Jalife, J. (1994), 'Thinning of the myocardial wall as an attractor of vortex-like reentry in a 3-dimensional model of cardiac excitation', *Circulation* **90**(4 Pt2), 519.

Pertsov, A. M., Davidenko, J. M., Salomonsz, R., Baxter, W. & Jalife, J. (1993), 'Spiral waves of excitation underlie reentrant activity in isolated cardiac muscle', *Circ. Res.* **73**(3), 631–650.

Vinson, M. (1998), 'Interactions of spiral waves in inhomogeneous excitable media', *Physica D* **116**(3–4), 313–324.

Vinson, M., Pertsov, A. & Jalife, J. (1994), 'Anchoring of vortex filaments in 3D excitable media', *Physica D* **72**(1–2), 119–134.

Winfree, A. T. (1991), 'Alternative stable rotors in an excitable medium', *Physica D* **49**(1–2), 125–140.

Winfree, A. T. (1994), 'Electrical turbulence in 3-dimensional heart muscle', *Science* **266**(5187), 1003–1006.

Witkowski, F. X., Leon, L. J., Penkoske, P. A., Giles, W. R., Spano, M. L., Ditto, W. L. & Winfree, A. T. (1998), 'Spatiotemporal evolution of ventricular fibrillation', *Nature* **392**, 78–82.

Xie, F., Qu, Z., Weiss, J. N. & Garfinkel, A. (1999), 'Interactions between stable spiral waves with different frequencies in cardiac tissue', *Phys. Rev. E* **59**, 2203–2205.

Zaitsev, A. V., Berenfeld, O., Jalife, J., Mironov, S. F. & Pertsov, A. M. (2000), 'Distribution of excitation frequencies on the epicardial and endocardial surfaces of fibrillating ventricular walls of the sheep heart', *Circ. Res.* **86**(4), 408–417.

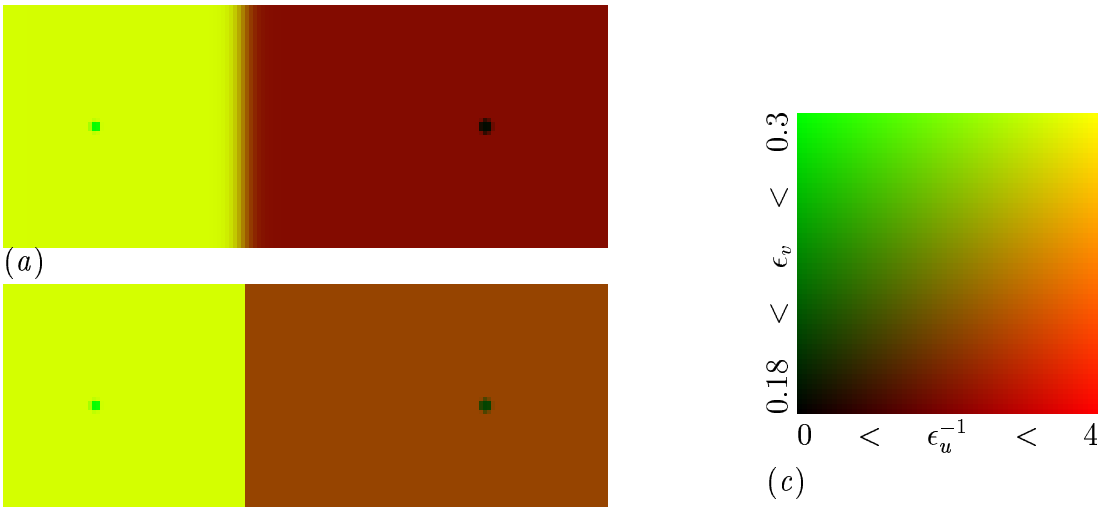

Figure 1: Colour-coded spatial distribution of the parameters ϵ_u and ϵ_v in numerical experiments. (a) Smooth inhomogeneity, $k \approx 1.618$, $w = 3$. Two localised defects seen as the dark (green) spots are regions of reduced excitability, *i.e.* high value of ϵ_u. (b) Weaker and sharp, stepwise inhomogeneity, $k \approx 1.414$, $w = 0$. (c) Colour coding of panels (a) and (b): the red component is determined by the value of ϵ_u^{-1} and the green component is determined by the value of ϵ_v.

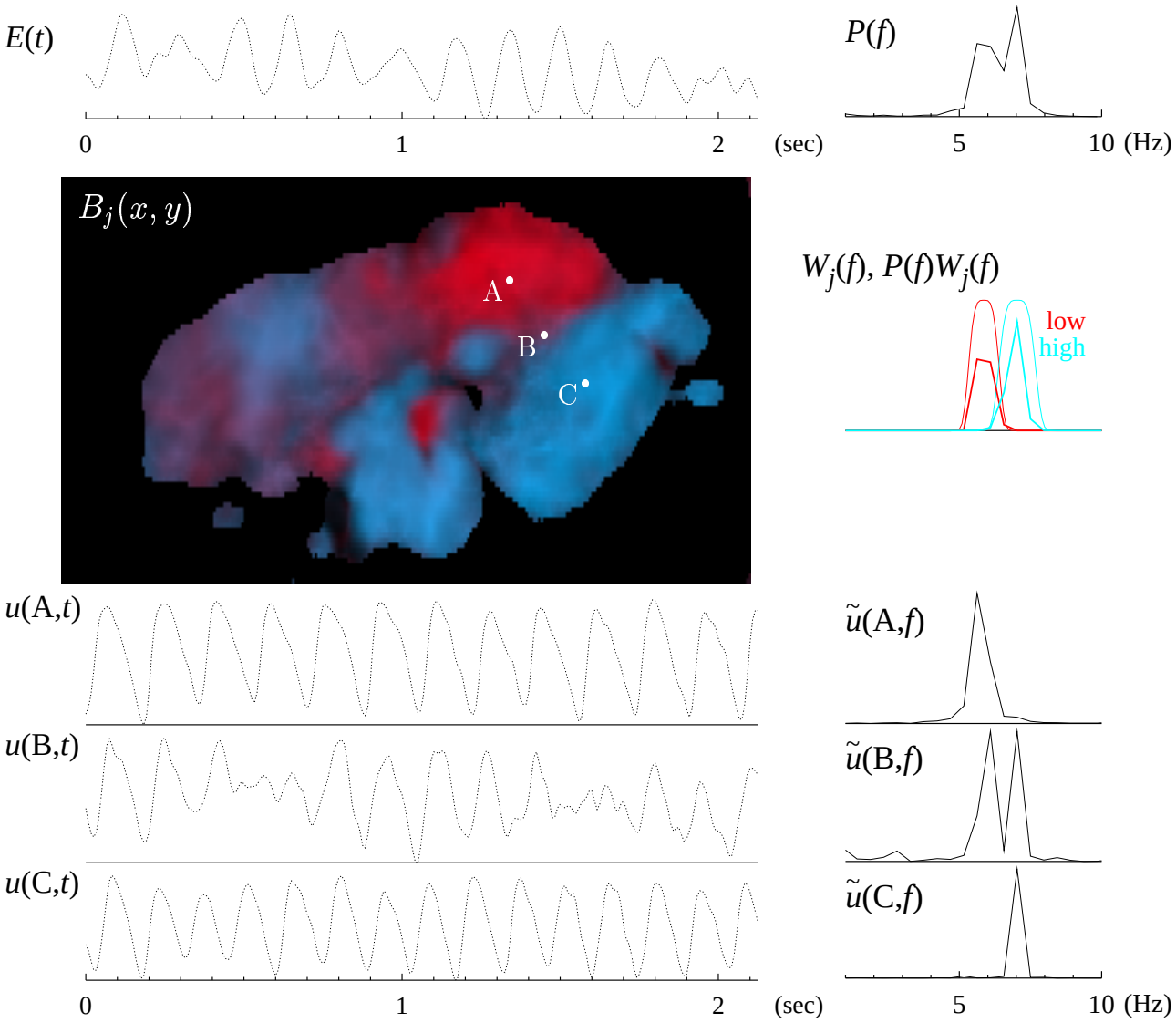

Figure 2: Frequency domains in an experimental polymorphic tachycardia/fibrillation. Top row: pseudo-ECG $E(t)$ (5), and cumulative power spectrum $P(f)$ (7). Below the cumulative spectrum: the filtering windows W_j (thin lines) and cumulative power spectra of the filtered signals PW_j (thick lines), lower frequency component (red) and higher frequency component (blue). The colour panel: $B_j(x,y)$ (9), the distribution of the power of the frequency bands through the preparation, blue component shows the power of the higher frequency and red component shows the power of the lower frequency. The spatial separation of the colours is the demonstration of the domain structure of the excitation pattern. Below: records $u(,t)$ and corresponding power spectra $\tilde{u}(,f)$ at points A, B and C shown on the frequency domains map. Frequency is in Hz, time is in seconds, vertical axes are in arbitrary units.

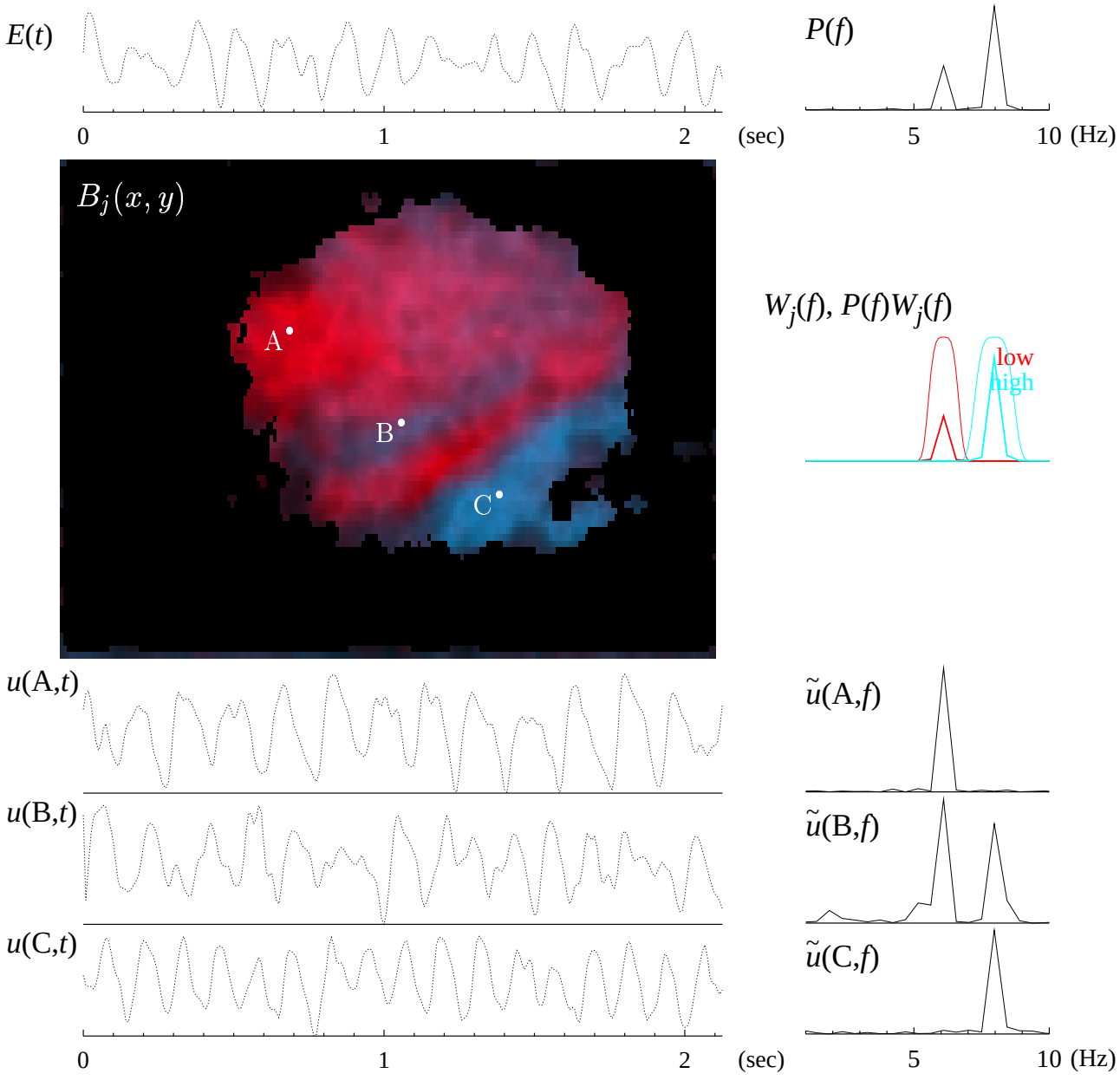

Figure 3: Another experimental polymorphic tachycardia/fibrillation. Same data format as in Fig. 2.

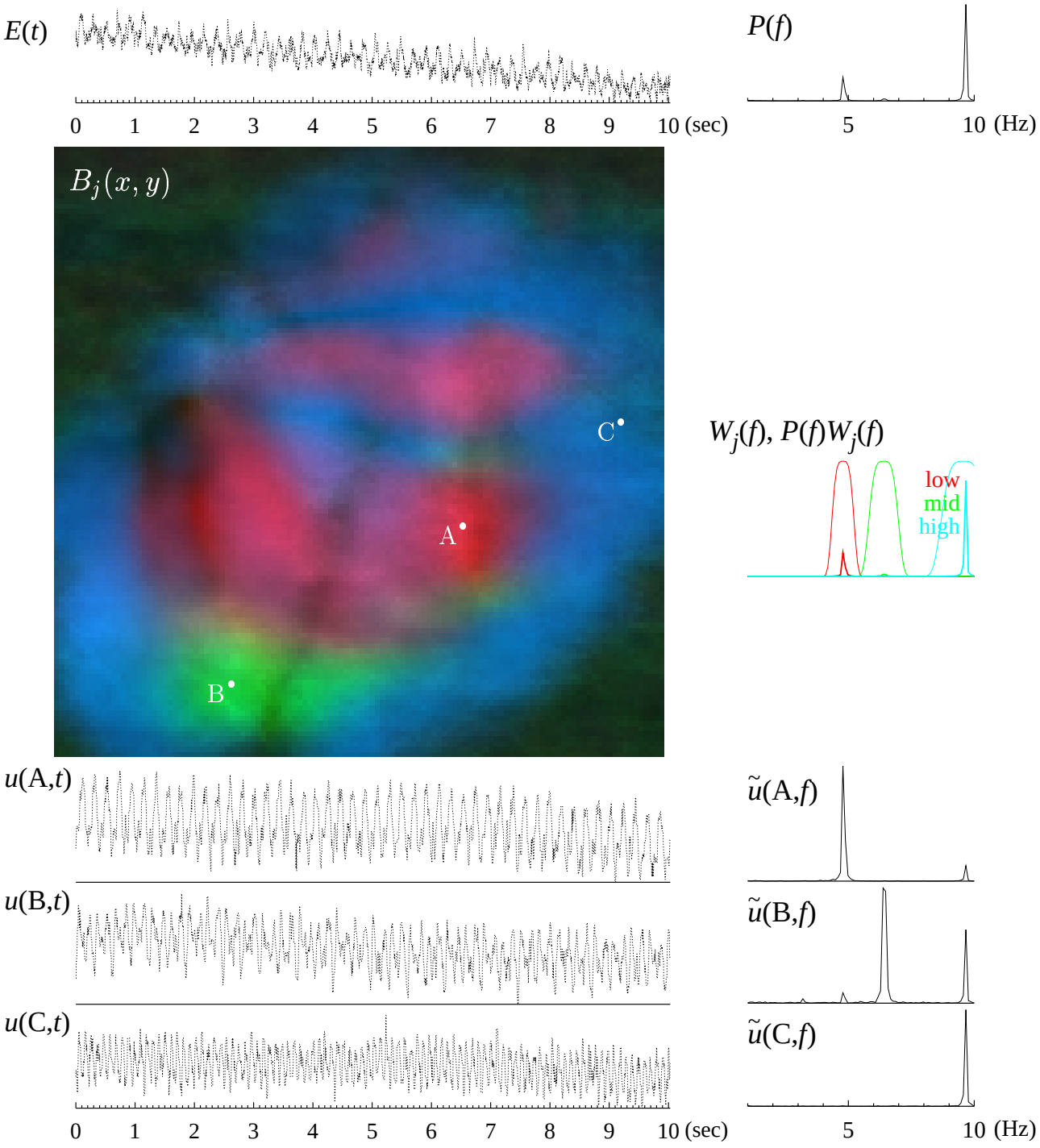

Figure 4: Frequency domain structure in a long-time experimental series with a complicated fibrillatory pattern. Here there are three frequency bands and correspondingly three domains, shown by red, green and blue; otherwise data format is the same as in Fig. 2.

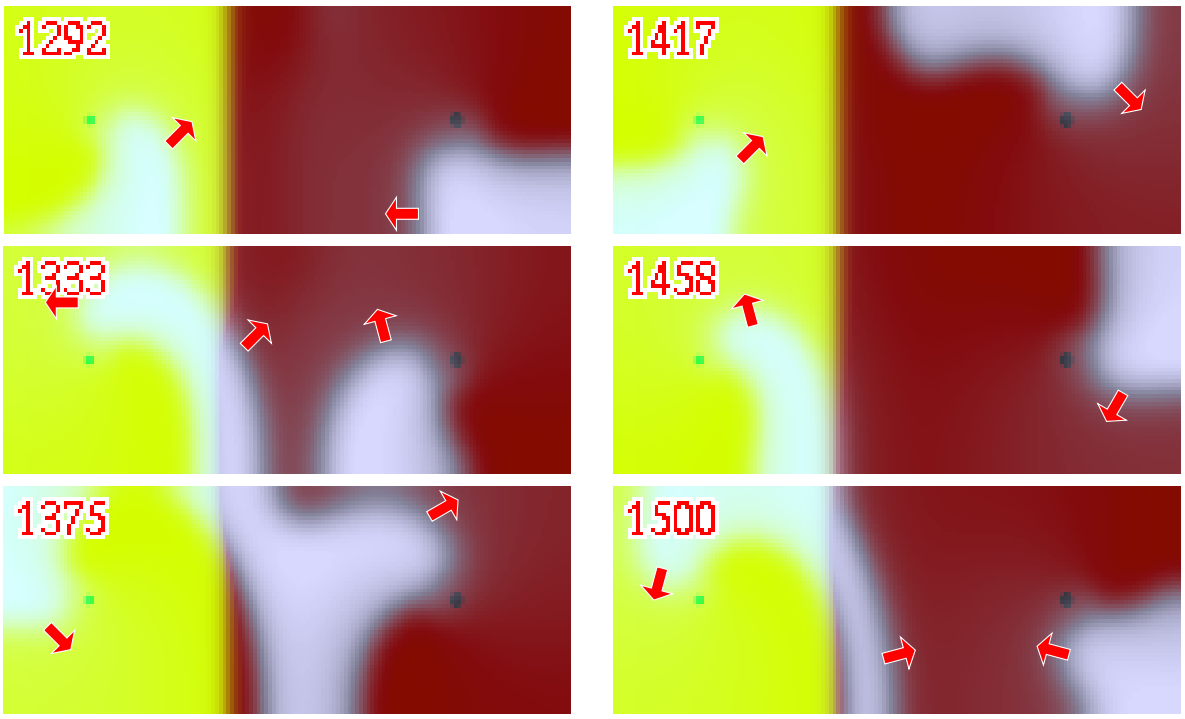

Figure 5: Snapshots of a fibrillatory excitation pattern produced by two spiral waves with incommensurate frequencies, in the numerical experiment. The fast spiral is in the left part of the medium, the slow spiral is in the right part. Colour coding: the background is the distribution of the parameters as on Fig. 1; the excitation wave is shown light-blue upon it. The red arrows show the direction of propagation of the waves. Labels show time in milliseconds. Parameters: $k \approx 1.618$, $w = 3$, corresponding to panel (a) of Fig. 1. The thin wave that just entered into the slow right part on panel 1500ms will decay before it meets the wave of the right spiral.

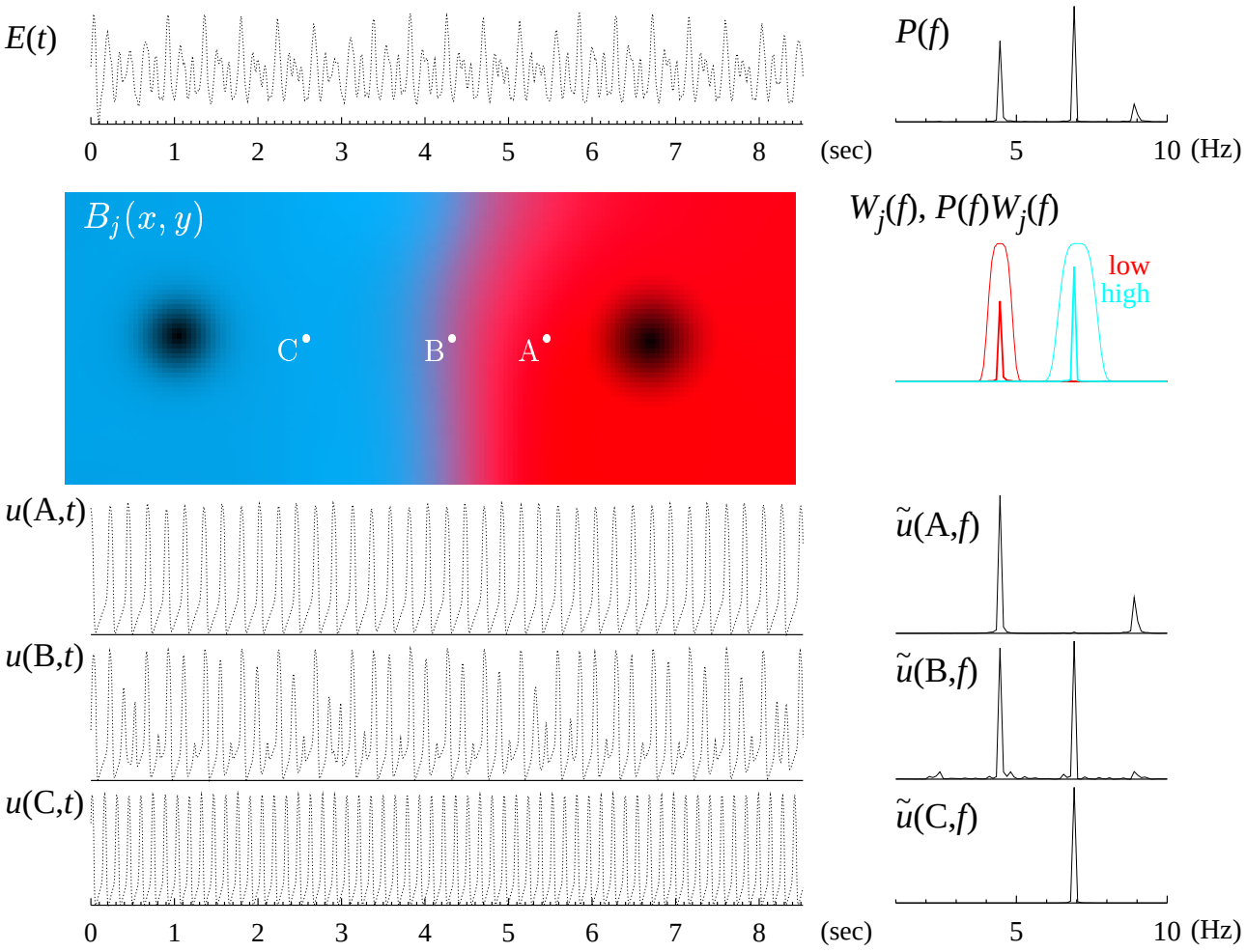

Figure 6: Frequency domain organisation of the numerical fibrillatory pattern shown on Fig. 5. Numerical data processed in the same way as the real experimental data of Figs. 2 and 3.

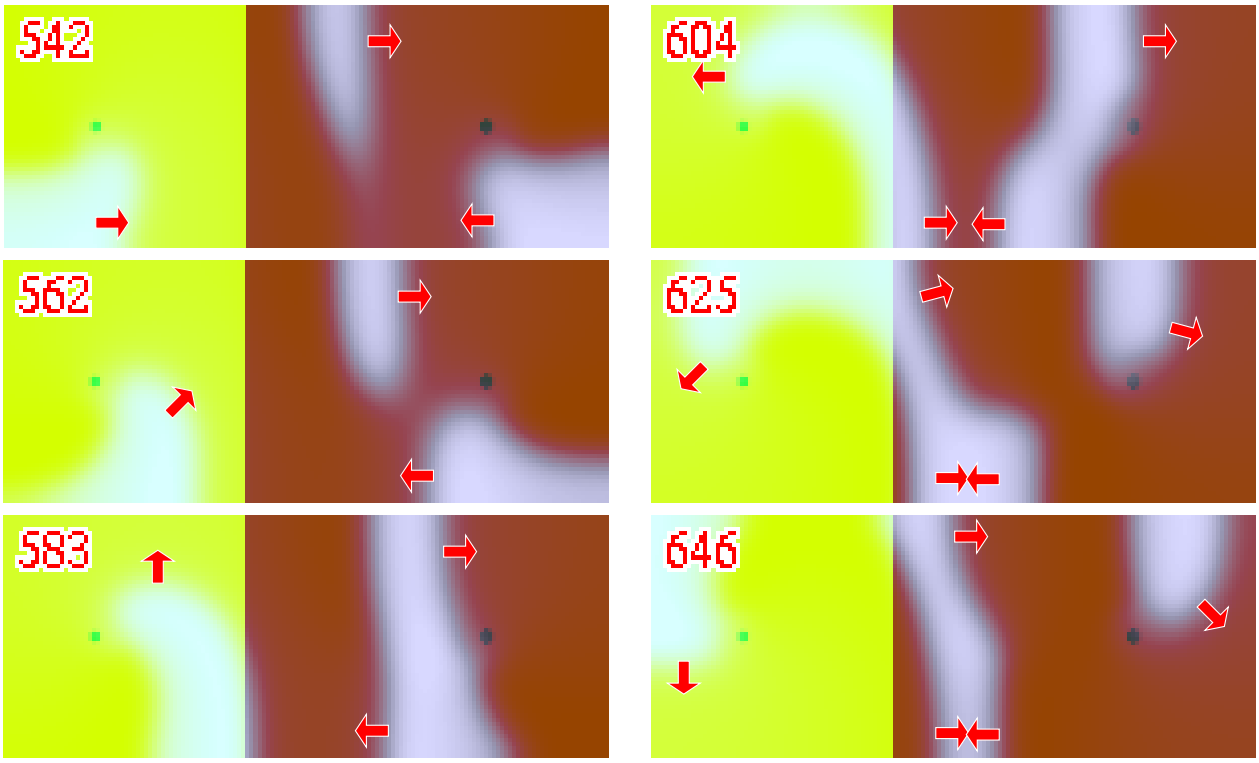

Figure 7: Fibrillatory pattern in a numerical experiment with the weaker inhomogeneity, corresponding to panel (b) of Fig. 1. There are two spiral waves. The faster waves from the left spiral sometimes penetrate to the right part, perturbing the rotation of the slow spiral, as shown on the selected sequence of snapshots; but as the right spiral is pinned to the inhomogeneity, it persists. The slow spiral in the right half existed for 4.2 sec.

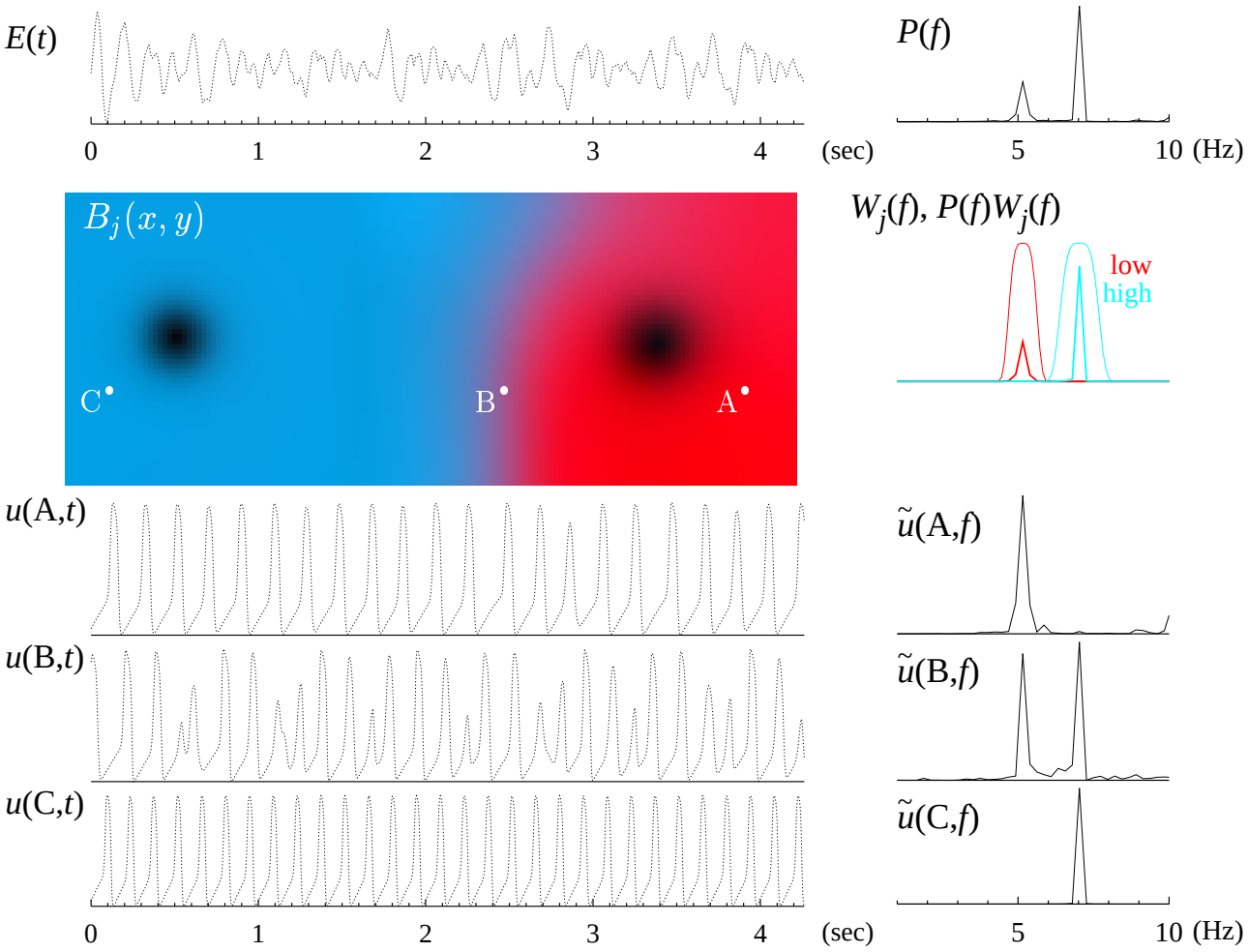

Figure 8: Frequency domain organisation of the pattern of Fig. 5.

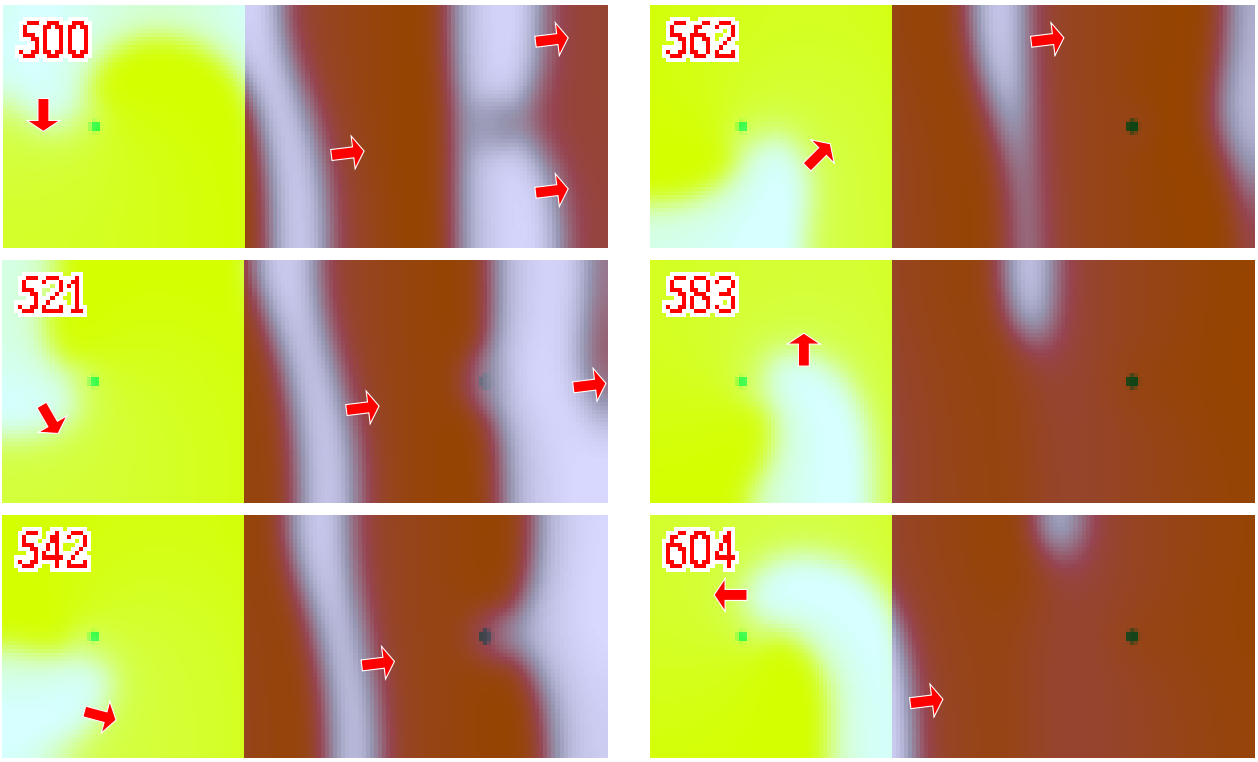

Figure 9: Continuation of the numerical experiment of Fig. 7, 8, after the slow spiral wave in the right part was annihilated. Now the right part is demonstrating 2:3 frequency division. The chosen sequence shows one passed wave and one decayed wave. The time labels are relative to the moment of annihilation of the slow spiral.

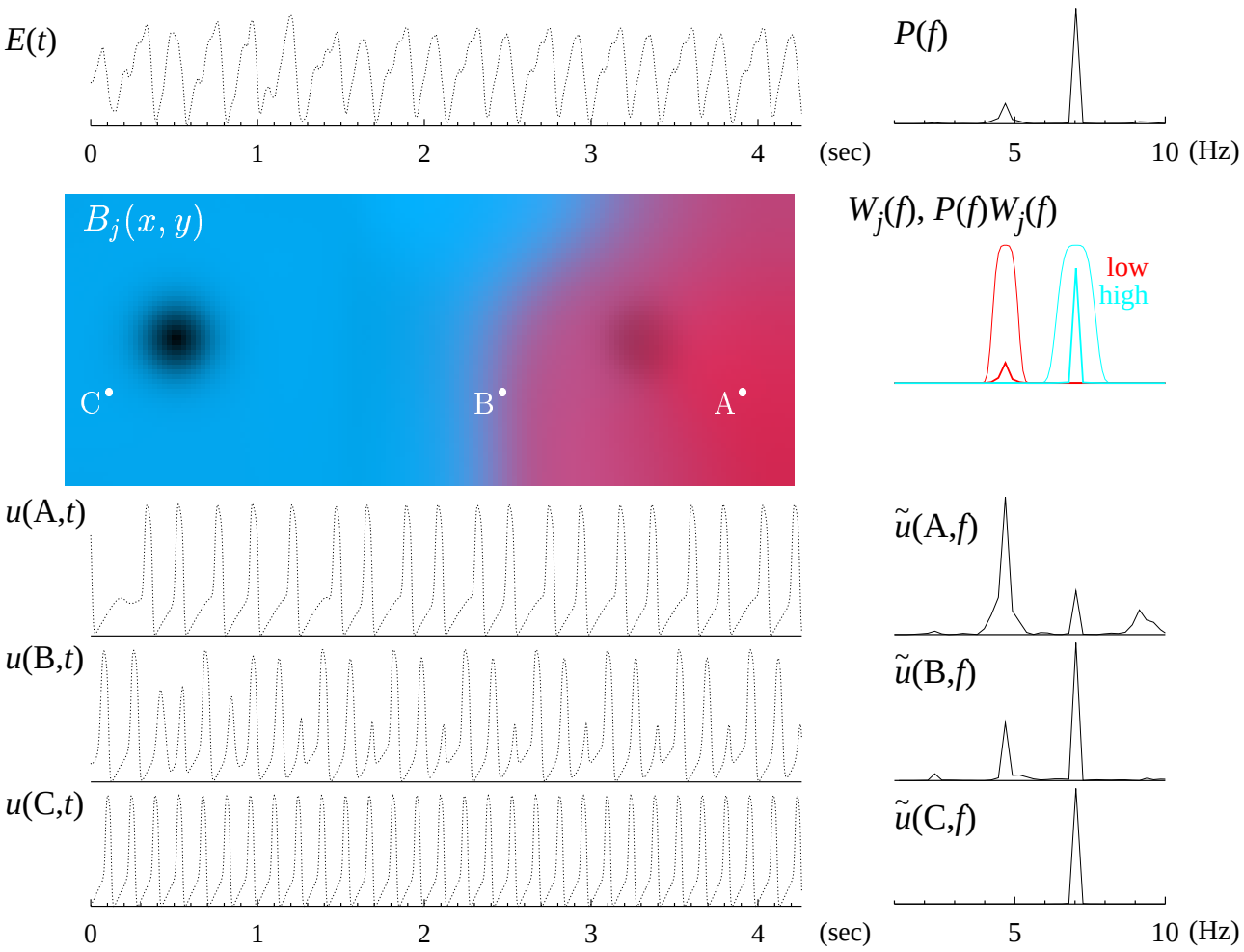

Figure 10: Frequency domain organisation after the annihilation of the slow spiral, corresponding to Fig. 9.

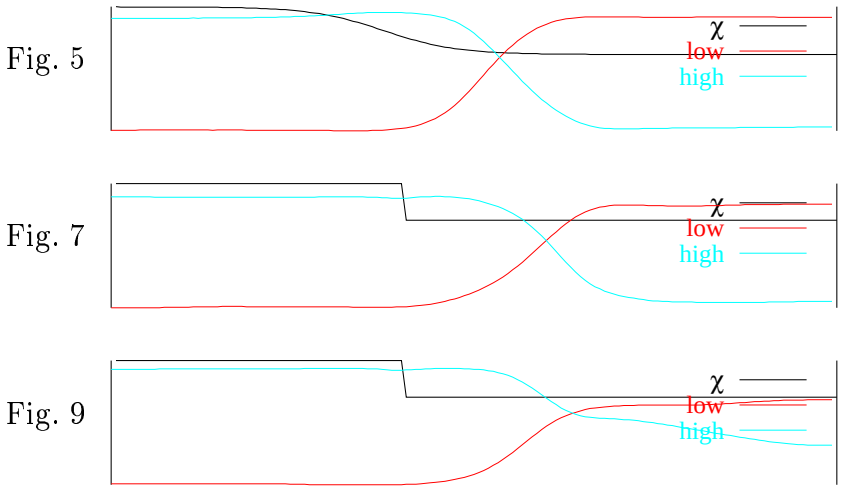

Figure 11: Profiles of the medium inhomogeneity $\chi(x)$, and of the amplitudes of frequency bands along the lower edge, $B_j(x, 0)$, for the three numerical experiments.

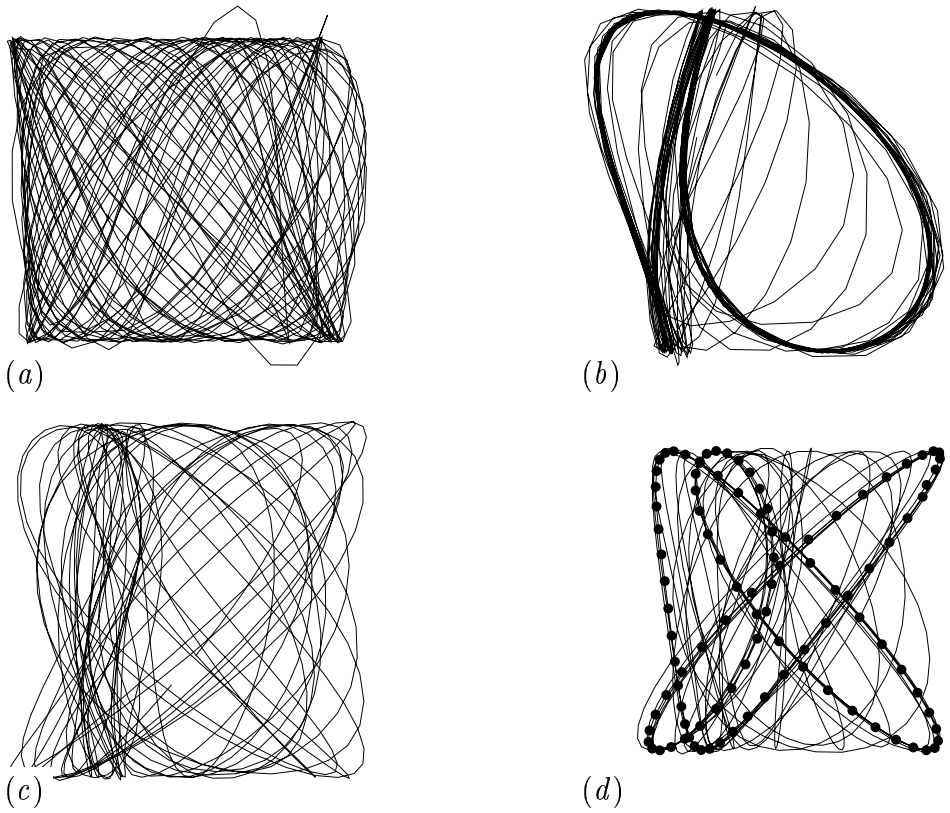

Figure 12: Lissajous curves of numerical experiments: (c) Fig. 6, two spirals, (d) 2:1 Wenckebach mechanism in the same model as Fig. 6, (e) Fig. 8, two spirals, and (f) Fig. 10, 2:3 Wenckebach with a transient. On each graph, the abscissa is record A and the ordinate is record C of the corresponding filtered experimental or numerical series. The filled circles on panel (d) are to emphasise the main Lissajous figure compared to the deviations from it due to the transient.

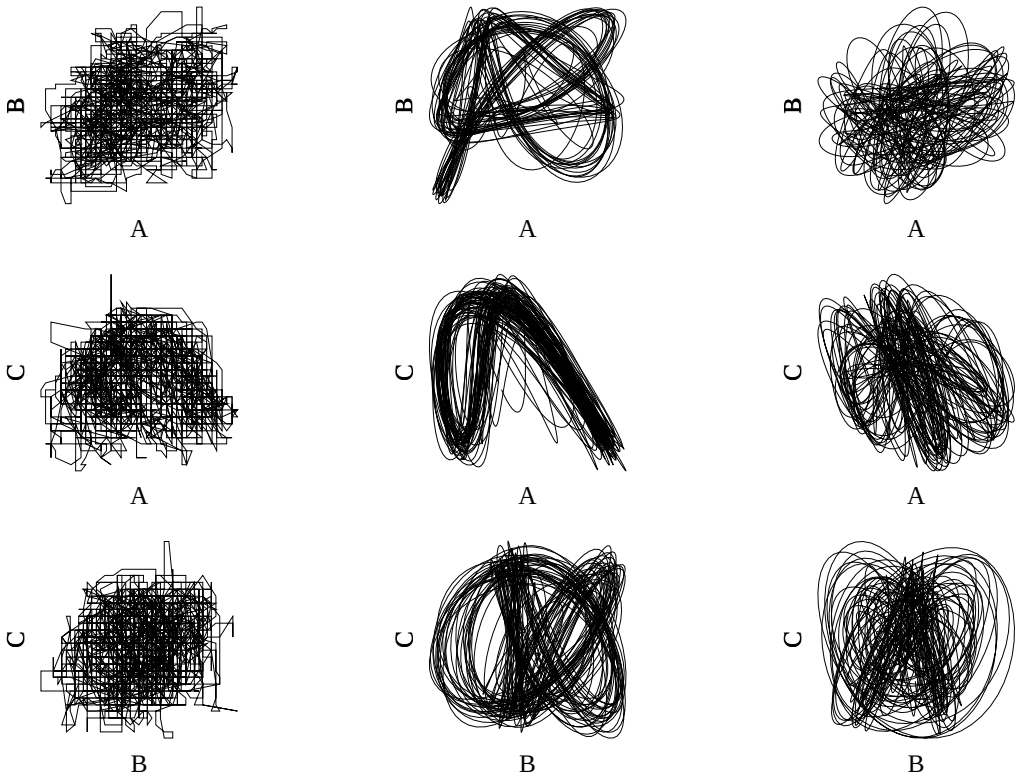

Figure 13: Lissajous figures of the recordings A, B and C of Fig. 4. Left column: raw data. Middle column: filtered data. Right column: filtered data with randomised phases.